Upscaling transformation plasticity using full field fast Fourier transform simulations of polycrystals undergoing phase transformations under applied loads

Shahul-Hameed Nambiyankulam-Hussain, Daniel Weisz-Patrault, Benoît Appolaire, Sabine Denis, Amico Settefrati

Upscaling transformation plasticity using full field fast Fourier transform simulations of polycrystals undergoing phase transformations under applied loads

Shahul Hameed Nambiyankulam Hussain[a,b,d], Daniel Weisz-Patrault[a,*], Benoit Appolaire[b,c], Sabine Denis[b,c], Amico Settefrati[d]

[a]*Laboratoire de Mécanique des Solides, CNRS, Ecole Polytechnique, Institut Polytechnique de Paris, Palaiseau, France*
[b]*Institut Jean Lamour, CNRS, Université de Lorraine, Nancy, France*
[c]*Laboratory of Excellence- Design of Alloy Metals for Low-mass Structures (DAMAS), Université de Lorraine, Nancy, France*
[d]*ArcelorMittal Global R&D, Maizières Process, Maizières-lès-Metz, France*

Abstract

Transformation plasticity has been intensively studied because of its significant impact on various industrial fabrication and forming processes. The widely used analytical macroscopic models are based on idealized microstructures and strong assumptions. Such models predict linear (or weakly non-linear) dependence between the transformation plastic strain rate and the applied load, whereas experimental evidence shows that this dependence becomes highly non-linear when the applied stress becomes non-negligible with respect to the macroscopic yield stress. Such a non-linear response is not fully understood especially for phase transformations arising at high temperatures for which the product phase is often softer than the parent phase, and involving visco-plastic behavior.

Therefore to overcome this difficulty, the first key contribution of this paper is to exhibit the detailed mechanisms leading to transformation plasticity in steels undergoing austenite to ferrite phase transformation at high temperature and to explain the non-linear dependence between the transformation plastic strain and the applied load. To do so, full-field simulations of visco-plastic polycrystalline aggregates undergoing phase transformations under applied load are performed. In addition, the second key contribution consists in upscaling the outcomes obtained at the scale of the polycrystal into a macroscopic statistical model, that can be used for large simulations of industrial processes. To do so, a database of computations with various initial microstructures, grain shape distributions, and applied loads have been performed, and used to derive the macroscopic statistical model. Of course, to create such a database, a relatively short computation time should be obtained for the full-field simulations, which is achieved by using a fast Fourier transform-based algorithm.

Keywords: Transformation plasticity, Up-scaling, Fast Fourier transform

*Corresponding author e-mail: daniel.weisz-patrault@cnrs.fr

1. Introduction

Transformation plasticity is the average plastic strain that arises when metals undergo solid-state phase transformations under applied loads. This phenomenon is of particular importance for the steel-making industry because solid-state transformations often occur under applied stress during welding [1], run-out-table [2] and coiling [3] processes, which significantly contributes to the formation of residual stresses leading to major issues such as flatness defects [4], coil sagging [5, 6] etc. Therefore, transformation plasticity has been intensively studied in the context of relatively low-temperature phase transformations where the product phase is harder than the parent phase (i.e., martensitic and bainitic phase transformations). Indeed, a significant amount of experimental evidences has been reported [7–11], and various theoretical or numerical models based on idealized microstructures and simple mechanisms have been established [12–27].

On this basis, the main mechanisms leading to transformation plasticity have been identified and traditionally divided into Greenwood & Johnson [28] and Magee [29] mechanisms. When solid-state phase transformation occurs, the product phase is subjected to a significant eigenstrain corresponding to the atomic rearrangement (isotropic and deviatoric parts), which therefore depends on the crystal orientation of the product phase. Such an eigenstrain locally induces a non-negligible plastic flow even though there is no applied macroscopic load. However, if crystal orientations are isotropically distributed and the grains are more or less spherical, the average plastic flow over a large number of grains vanishes. Indeed, in this situation the eigenstrains and hence the induced plastic strains are isotropically distributed over all the forming grains of the product phase, and therefore average to zero. On the contrary, when macroscopic stress (even much smaller than the yield stress) is imposed during phase transformation the plastic flow does not average to zero, which is the very definition of transformation plasticity. Indeed, (i) the plastic strain tends to orientate according to the macroscopic stress principal directions so that the plastic strain is not isotropically distributed and does not average to zero (i.e., Greenwood & Johnson mechanism), and (ii) the crystal orientation of the forming grains may be preferentially selected according to the applied stress principal directions so that the corresponding eigenstrains are not isotropically distributed and hence the induced plastic flow does not average to zero (i.e., Magee mechanism).

Although widely used, simple analytical models such as [13] are limited to small applied stress in comparison to the yield stress as a linear (or a weakly non-linear [27]) dependence with respect to the applied load is typically obtained, whereas experimental evidence clearly shows strongly non-linear behavior for applied stress higher than half of the yield stress. Therefore, full field computations at the mesoscopic scale (i.e., polycrystal) have been performed including low-temperature phase transformations and crystal plasticity [30–33] and detailed mechanisms explaining transformation plasticity have been identified.

However, for high-temperature phase transformation in steels, the parent phase (i.e., γ-austenite) is harder than the product phase (i.e., α-ferrite) [34], which significantly modifies the local mechanisms proposed in previous studies based on full field computations [31–33] and the overall analytical formulas [13, 26, 27]. Therefore, the key contribution of this paper is to perform full-field simulations of polycrystals for different applied loads while undergoing high temperature $\gamma \rightarrow \alpha$ phase transformation where the product phase is softer than the parent phase. On this

basis, the local mechanisms responsible for transformation plasticity are identified. In addition, a statistical upscaling strategy is proposed, which is comparable to previous studies [35, 36] within the framework of grain growth during annealing. To do so, a database of computations is created to derive a macroscopic statistical model including the non-linear dependence of transformation plasticity with respect to the applied load. Full-field computations should therefore be relatively fast, and a fast Fourier transform (FFT) approach [37] is chosen for the full-field simulations of periodic polycrystals.

The present work presents several significant differences in comparison to previous studies [31–33] (focusing on transformation plasticity during low-temperature phase transformation). Indeed, since high-temperature phase transition is considered in this paper, an isotropic visco-plastic behavior (i.e., independent of crystal orientation) is used instead of crystal plasticity (i.e., strongly dependent on crystal orientation). In addition, in this contribution, the complete Bain strain (i.e., isotropic and deviatoric part) is considered for the eigenstrain imposed in the forming phase, whereas only the volume change was taken into account in previous studies.

The paper is organized as follows. Mesoscopic scale full field simulations are presented in section 2. Results are analyzed in section 3 to provide the detailed mechanisms leading to transformation plasticity and derive the statistical upscaling strategy accounting for the non-linear dependence of the transformation plastic strain with respect to the applied stress. Conclusive remarks are provided in section 4.

2. Mesoscopic scale simulations

In this section, theoretical foundations and assumptions underlying the full-field simulations at the mesoscopic scale are detailed. As already mentioned a FFT-based algorithm is developed to reach short computation time. Consequently, representative volume elements (RVE) are periodic Voronoi tessellations contained in cubic unit cells, which are rasterized onto regular grids. Initially, all grains are face-centered cubic (FCC) (i.e., γ-austenite), and crystal orientation is randomly assigned to each grain. The γ-austenite to α-ferrite phase transformation is then considered under isothermal conditions at 750°C. Phase transformation is simulated by randomly selecting N nuclei among the voxels lying on grain boundaries, and applying spherical growth according to a specific growth rate denoted by g (voxels.s^{-1}). It should be noted that periodic conditions are conserved during grain growth. Crystal orientations of the forming grains are determined: (i) by randomly selecting from which side of the grain boundary the grain nuclei inherit its crystal orientation, and (ii) by randomly selecting one of the three possible variants according to the Bain transformation. At each time increment, the eigenstrain corresponding to the Bain transformation is imposed on all the voxels that changed phase (i.e., $\gamma \rightarrow \alpha$) between the previous and the current time step. Boundary conditions consist of macroscopic tension so that the applied second-order stress tensor $\boldsymbol{\Sigma}$ reads $\boldsymbol{\Sigma} = \Sigma\, \boldsymbol{e}_1 \otimes \boldsymbol{e}_1$ where $\boldsymbol{e}_1$ is one of the unit cell direction and where $\Sigma \in \mathbb{R}$ and where:

$$\boldsymbol{\Sigma} = \frac{1}{V} \int_V \boldsymbol{\sigma}(\boldsymbol{x})\, \mathrm{d}V \tag{1}$$

where V is the volume of the RVE, and where at the mesoscopic scale $\boldsymbol{\sigma}$ is the local Cauchy stress second-order tensor and $\boldsymbol{x}$ denotes the local coordinates.

Elasto-viscoplasticity is considered for both phases. The elastic stiffness tensor is anisotropic according to the cubic symmetry, and an isotropic Chaboche viscoplastic constitutive law is considered [38]. Material coefficients involved in the Chaboche law are identified for both phases by using experimental results [34]. As already mentioned austenite is harder than ferrite at $750°\mathrm{C}$, which significantly impacts the detailed mechanisms leading to transformation plasticity.

2.1. Local constitutive equations

At the mesoscopic scale, the local displacement vector field is denoted by $\boldsymbol{u}(\boldsymbol{x})$. The total local strain second-order tensor at mesoscale is denoted by $\boldsymbol{\varepsilon}$ is defined by:

$$\boldsymbol{\varepsilon}(\boldsymbol{x}) = \frac{1}{2}\left(\boldsymbol{\nabla}\boldsymbol{u}(\boldsymbol{x}) + \boldsymbol{\nabla}\boldsymbol{u}(\boldsymbol{x})^{\top}\right) \tag{2}$$

Under infinitesimal strain assumption, the total strain is composed of elastic $\boldsymbol{\varepsilon}^{\mathrm{e}}$, transformation (i.e., eigenstrain) $\boldsymbol{\varepsilon}^{*}$, and plastic $\boldsymbol{\varepsilon}^{\mathrm{p}}$ contributions such as:

$$\boldsymbol{\varepsilon}(\boldsymbol{x}) = \boldsymbol{\varepsilon}^{\mathrm{e}}(\boldsymbol{x}) + \boldsymbol{\varepsilon}^{*}(\boldsymbol{x}) + \boldsymbol{\varepsilon}^{\mathrm{p}}(\boldsymbol{x}) \tag{3}$$

It should be noted that since the isothermal condition is assumed in this paper, thermal expansion is not considered.

The local Cauchy stress tensor denoted by $\boldsymbol{\sigma}$ is related to the elastic strain tensor $\boldsymbol{\varepsilon}^{\mathrm{e}}$ with the fourth-order stiffness tensor $\boldsymbol{C}$, which is assumed to be uniform in each phase:

$$\boldsymbol{\sigma}(\boldsymbol{x}) = \boldsymbol{C}(\boldsymbol{x}) : \boldsymbol{\varepsilon}^{\mathrm{e}}(\boldsymbol{x}) \tag{4}$$

The eigenstrain due to phase transformation (volume variation and deviatoric parts) is explicitly given by the austenite-to-ferrite transformation mechanism. Among various existing mechanisms (i.e., Bain, Kurdjumov-Sachs, Nishiyama-Wassermann, etc.) the Bain austenite to ferrite transformation relation is considered in this contribution for the sake of simplicity, hence:

$$\boldsymbol{\varepsilon}^{*}(\boldsymbol{x}) = \left(\sqrt{2}\,\frac{a^{\gamma}}{a^{\alpha}} - 1\right)\left(\boldsymbol{e}_1^{\gamma}(\boldsymbol{x}) \otimes \boldsymbol{e}_1^{\gamma}(\boldsymbol{x}) + \boldsymbol{e}_2^{\gamma}(\boldsymbol{x}) \otimes \boldsymbol{e}_2^{\gamma}(\boldsymbol{x})\right) + \left(\frac{a^{\gamma}}{a^{\alpha}} - 1\right)\boldsymbol{e}_3^{\gamma}(\boldsymbol{x}) \otimes \boldsymbol{e}_3^{\gamma}(\boldsymbol{x}) \tag{5}$$

where $\boldsymbol{e}_1^{\gamma}, \boldsymbol{e}_2^{\gamma}, \boldsymbol{e}_3^{\gamma}$ are the local unit vectors of the ferrite crystal, and a^{γ} and a^{α} are lattice parameters of ferrite and austenite respectively. It should be noted that variants are obtained by permuting $\boldsymbol{e}_1^{\gamma}, \boldsymbol{e}_2^{\gamma}, \boldsymbol{e}_3^{\gamma}$. Hence using experimental data [39]:

$$\boldsymbol{\varepsilon}^{*}(\boldsymbol{x}) \approx 0.1119\,\left(\boldsymbol{e}_1^{\gamma}(\boldsymbol{x}) \otimes \boldsymbol{e}_1^{\gamma}(\boldsymbol{x}) + \boldsymbol{e}_2^{\gamma}(\boldsymbol{x}) \otimes \boldsymbol{e}_2^{\gamma}(\boldsymbol{x})\right) - 0.2138\,\boldsymbol{e}_3^{\gamma}(\boldsymbol{x}) \otimes \boldsymbol{e}_3^{\gamma}(\boldsymbol{x}) \tag{6}$$

The plastic strain is computed according to the flow rule:

$$\dot{\boldsymbol{\varepsilon}}^{\mathrm{p}}(\boldsymbol{x}) = \frac{3}{2}\left(\frac{\boldsymbol{\sigma}'(\boldsymbol{x}) - \boldsymbol{X}'(\boldsymbol{x})}{\sigma^{\mathrm{eq}}(\boldsymbol{x})}\right)\dot{p}_{\mathrm{cum}}(\boldsymbol{x}) \tag{7}$$

where $\boldsymbol{\sigma}'$ and $\boldsymbol{X}'$ are deviatoric parts of the Cauchy stress tensor $\boldsymbol{\sigma}$ and back stress tensor $\boldsymbol{X}$ respectively, σ^{eq} is the von Mises equivalent stress defined by:

$$\sigma^{\mathrm{eq}}(\boldsymbol{x}) = \sqrt{\frac{3}{2}\left(\boldsymbol{\sigma}'(\boldsymbol{x}) - \boldsymbol{X}'(\boldsymbol{x})\right) : \left(\boldsymbol{\sigma}'(\boldsymbol{x}) - \boldsymbol{X}'(\boldsymbol{x})\right)} \tag{8}$$

and $\dot{p}_{\text{cum}}$ is the cumulative plastic strain rate defined by:

$$\dot{p}_{\text{cum}}(\boldsymbol{x}) = \sqrt{\frac{2}{3}\,\dot{\boldsymbol{\varepsilon}}^{\text{p}}(\boldsymbol{x}) : \dot{\boldsymbol{\varepsilon}}^{\text{p}}(\boldsymbol{x})} \tag{9}$$

In addition, the Chaboche visco-plastic criterion reads:

$$\dot{p}_{\text{cum}}(\boldsymbol{x}) = \left(\frac{\sigma^{\text{eq}}(\boldsymbol{x}) - R_0(\boldsymbol{x}) - R(\boldsymbol{x})}{K(\boldsymbol{x})}\right)^{n(\boldsymbol{x})} \tag{10}$$

where R_0, R, K, and n are the initial yield stress, isotropic hardening coefficient, drag stress, and the exponent of the power law respectively. The isotropic and kinematic hardening laws are given by:

$$\dot{R}(\boldsymbol{x}) = b(\boldsymbol{x})\ \left(Q(\boldsymbol{x}) - R(\boldsymbol{x})\right)\dot{p}_{\text{cum}}(\boldsymbol{x}) \tag{11}$$

$$\dot{\boldsymbol{X}}(\boldsymbol{x}) = \frac{2}{3}\,C(\boldsymbol{x})\,\dot{\boldsymbol{\varepsilon}}^{\text{p}}(\boldsymbol{x}) - D(\boldsymbol{x})\,\boldsymbol{X}(\boldsymbol{x})\,\dot{p}_{\text{cum}}(\boldsymbol{x}) \tag{12}$$

where b, Q, C, D are material parameters at a given temperature. It should be noted that all material parameters are heterogeneous (i.e., depend on $\boldsymbol{x}$) as the domain is composed of austenite and ferrite phases each of which has specific material properties.

Hardening properties for both phases at $750°C$ are identified based on Liebaut [34] within the range 10^{-3} s^{-1} to 5×10^{-3} s^{-1} for the strain rate, which is realistic for the $\gamma \rightarrow \alpha$ phase transformation. However, the proposed FFT -based approach is limited to $n = 1$ to facilitate convergence, which induces a bias between the considered Chaboche law and hardening curves obtained in [34] as shown in Figure 1. However, the fitted Chaboche law is reasonable and would lead to identifying local mechanisms of transformation plasticity. Material parameters arising in the Chaboche law are listed in Table 1.

Table 1: Viscoplastic parameters for austenite and ferrite at $750°C$

Parameter		Austenite	Ferrite
b	(-)	50	100
R_0	(GPa)	0.012	0.014
Q	(GPa)	0.0555	0.0135
C	(GPa)	0.191	0.045
D	(GPa)	0.001	0.001
K	(GPa.s^{-1})	6	1.5
n	(-)	1	1

In addition, elastic properties are listed in Table 2, where the fourth-order stiffness tensor $\boldsymbol{C}$ reads with cubic symmetry:

$$\begin{aligned}\boldsymbol{C}(\boldsymbol{x}) = \ & (C_{11}^{\varphi} - C_{12}^{\varphi} - 2C_{44}^{\varphi})\left(\boldsymbol{e}_j^{\varphi}(\boldsymbol{x}) \otimes \boldsymbol{e}_j^{\varphi}(\boldsymbol{x}) \otimes \boldsymbol{e}_j^{\varphi}(\boldsymbol{x}) \otimes \boldsymbol{e}_j^{\varphi}(\boldsymbol{x})\right) \\ & + C_{12}^{\varphi}\left(\boldsymbol{e}_j^{\varphi}(\boldsymbol{x}) \otimes \boldsymbol{e}_j^{\varphi}(\boldsymbol{x}) \otimes \boldsymbol{e}_k^{\varphi}(\boldsymbol{x}) \otimes \boldsymbol{e}_k^{\varphi}(\boldsymbol{x})\right) \\ & + C_{44}^{\varphi}\left(\boldsymbol{e}_j^{\varphi}(\boldsymbol{x}) \otimes \boldsymbol{e}_k^{\varphi}(\boldsymbol{x}) \otimes \left(\boldsymbol{e}_k^{\varphi}(\boldsymbol{x}) \otimes \boldsymbol{e}_j^{\varphi}(\boldsymbol{x}) + \boldsymbol{e}_j^{\varphi}(\boldsymbol{x}) \otimes \boldsymbol{e}_k^{\varphi}(\boldsymbol{x})\right)\right)\end{aligned} \tag{13}$$

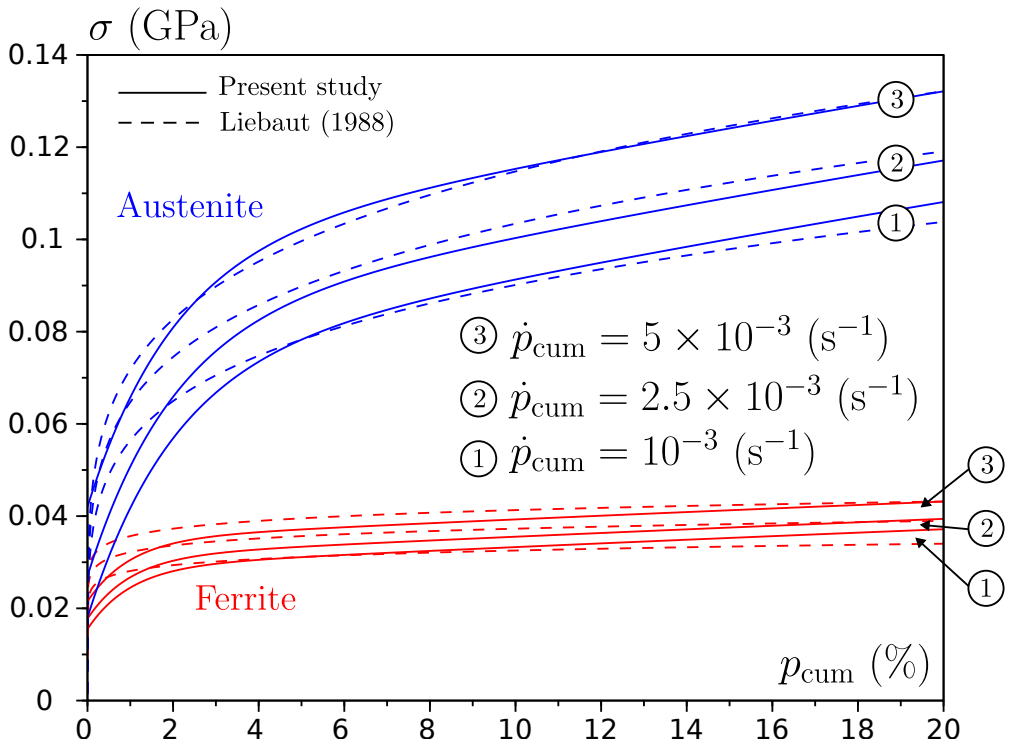

Figure 1: Hardening curves for a uniaxial test at different strain rates for austenite and ferrite.

Where sums are implicitly considered over j and k indexes (with $1 \leq j \leq 3$ and $1 \leq k \leq 3$), the exponent φ should be replaced by α for austenite grains and by γ for ferrite grains, $C^{\gamma}_{11}, C^{\gamma}_{12}, C^{\gamma}_{44}$ and $C^{\alpha}_{11}, C^{\alpha}_{12}, C^{\alpha}_{44}$ are elastic constant in ferrite and austenite respectively, and $\boldsymbol{e}^{\gamma}_1, \boldsymbol{e}^{\gamma}_2, \boldsymbol{e}^{\gamma}_3$ and $\boldsymbol{e}^{\alpha}_1, \boldsymbol{e}^{\alpha}_2, \boldsymbol{e}^{\alpha}_3$ are the local unit vectors of the ferrite and austenite crystals respectively.

Table 2: Cubic elastic constants for austenite and ferrite at $750°C$

Parameter		Austenite	Ferrite
C_{11}	(GPa)	117.4	162.8
C_{12}	(GPa)	74.8	127
C_{44}	(GPa)	110.9	100
ρ	(Kg.m^{-3})	7608	7386.4

2.2. FFT full-field simulations

As already mentioned to reach short computation time, a FFT-based algorithm is used to solve the elasto-visco-plastic full field problem composed of polycrystalline aggregates undergoing phase transformation under applied loads. The classical scheme proposed by [40] is used, which involves using periodic cubic cells composed of voxels to represent the polycrystalline RVEs. For the initial austenite polycrystalline aggregates, classical periodic Voronoi-Laguerre tessellations are generated using Neper [41] to easily control the grain shape distribution. Tessellations with $N_{\text{aus}} = 100$ austenite grains are considered and crystal orientation is randomly assigned with a

uniform distribution. Resulting tessellations are then rasterized (i.e., approximated by a voxels division) to be used as geometrical support of the FFT-based algorithm.

Phase transformation is simulated by randomly selecting $N_{\text{fer}} = 100$ nuclei for ferrite grains as individual voxels belonging to austenite grain boundaries (GB) as ferrite grains are known to often nucleate from GBs. Then all nuclei are grown spherically at a given rate g (voxel.s^{-1}) so that:

$$\dot{r} = g \tag{14}$$

where r (voxels) is the time-dependent radius of the growing ferrite grain. In practice, the growth rate g has been fixed to $g = 0.06$ voxels.s^{-1} so that the volume phase fraction of ferrite grains V_f roughly reaches 65% within 130 s, which is consistent with experimental data of ferrite phase transformation [34]. Of course, depending on the ferrite nuclei distribution, the phase transformation kinetics is different in all RVEs.

In addition, phase transformation involves the crystal orientation of ferrite grains. Various orientation relationships (e.g., Bain, Kurdjumov-Sachs, Nishiyama-Wassermann, etc.) enable to determine the crystal orientation of ferrite nuclei. In this contribution since the Bain mechanism has been selected for the transformation strain $\boldsymbol{\varepsilon}^*$, the Bain orientation relationship is also used. Therefore the frame of each ferrite nuclei is rotated by 45° with respect to the parent austenite grains around one of the three directions of the austenite frame. Hence the orientation matrix between austenite and ferrite reads:

$$O = \begin{pmatrix} \frac{1}{\sqrt{2}} & -\frac{1}{\sqrt{2}} & 0 \\ \frac{1}{\sqrt{2}} & \frac{1}{\sqrt{2}} & 0 \\ 0 & 0 & 1 \end{pmatrix} \tag{15}$$

In practice, since ferrite grain nuclei are created at GBs of the austenite grains, the parent austenite grain from one side of the grain GB is randomly selected, and then one of the three possible variants of the orientation matrix (15) is randomly selected to determine the crystal orientation of the ferrite growing grain.

It should be noted that at each time step during phase transformation the RVE remains periodic so that the FFT based-algorithm applies, and the transformation strain (i.e., eigenstrain $\boldsymbol{\varepsilon}^*$) is applied in voxels that have been switched from austenite to ferrite between the previous and the current time step. The RVE undergoing phase transformation with the associated mechanical problem including applied stress as boundary conditions and eigenstrain is depicted in Figure 2 to summarize the full-field simulation.

2.3. Transformation plasticity

By definition transformation plasticity is the volume average plastic strain over the entire RVE when an external load is applied during phase transformation. Hence the transformation plastic strain second-order tensor $\boldsymbol{E}^{\text{tp}}$ reads as the following volume average:

$$\boldsymbol{E}^{\text{tp}} = \frac{1}{V} \int_V \boldsymbol{\varepsilon}^{\text{p}}(\boldsymbol{x}) \, \mathrm{d}V \tag{16}$$

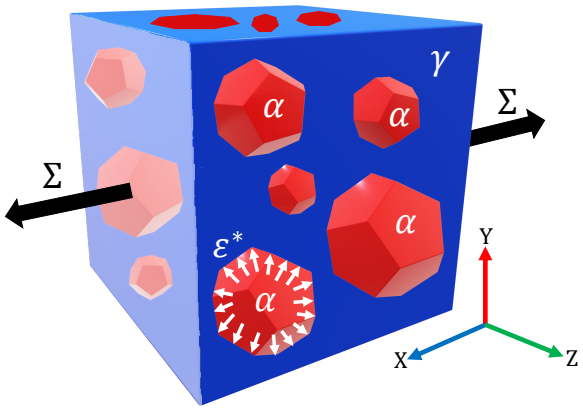

Figure 2: Boundary condition of the RVE with macroscopic external stress (uniaxial tension) Σ and Bain transformation strain ε^* over the evolving product phase grains.

where V is the volume of the RVE. The average cumulative plastic strain rate denoted by $\dot{P}_{\text{cum}}$ is also defined as:

$$\dot{P}_{\text{cum}} = \sqrt{\frac{2}{3}\dot{\boldsymbol{E}}^{\text{tp}} : \dot{\boldsymbol{E}}^{\text{tp}}} \tag{17}$$

In the following partial volume average over ferrite grains or austenite grains only will also be considered that is to say that the average is considered over V_{aus} and V_{fer} representing the volume occupied by austenite and ferrite grains respectively.

3. Results and discussion

3.1. Database

A total of 12 periodic-oriented tessellations initially composed of austenite grains with different grain morphology (see, for instance, Figure 3) are included in the database. For each oriented tessellation, a $\gamma \rightarrow \alpha$ phase transformation is imposed under various macroscopic uniaxial tension/compression such as $\boldsymbol{\Sigma} = \Sigma\, \boldsymbol{e}_1 \otimes \boldsymbol{e}_1$ is applied, where $\boldsymbol{e}_1, \boldsymbol{e}_2, \boldsymbol{e}_3$ are orthonormal directions defining the cubic cell (i.e., RVE), and Σ scans the following dataset given in GPa:

$$\Sigma \in \{-0.1, -0.075, -0.05, -0.025, -0.01, 0, 0.01, 0.025, 0.05, 0.075, 0.1\} \tag{18}$$

Hence a total of 132 computations are included in the database, discretized with 1452 time steps. To avoid storing massive data, only 11 time steps are extracted from each computation.

It should be noted that even though stress triaxiality of the applied load is not studied in this paper, the proposed methodology would be similar, but lead to a larger database. Since $\boldsymbol{\Sigma} = \Sigma\, \boldsymbol{e}_1 \otimes \boldsymbol{e}_1$ only the first principal component of the average plastic strain tensor will be studied in the following because $E^{\text{tp}}_{22} \approx E^{\text{tp}}_{33} \approx -E^{\text{tp}}_{11}/2$ and $E^{\text{tp}}_{12} \approx E^{\text{tp}}_{13} \approx E^{\text{tp}}_{23} \approx 0$.

3.2. Average response and transformation plasticity

As already mentioned, phase transformation is simply imposed by using a constant growth rate from randomly selected nuclei located at grain boundaries. Figure 4 depicts several cross

sections at the initial and final states (i.e., $t = 0$ with $V_f = 0\%$ and $t = 130$ s with $V_f \geq 65\%$ respectively). Austenite grains are shown in colors, and ferrite grains in white. In addition, Figure 5(a) illustrates the evolution of austenite and ferrite phase fractions over time for one particular oriented tessellation. This trend under isothermal conditions (i.e., at $T = 750°C$) is consistent with experimental data [42], which indicates that the simple strategy consisting in imposing phase transformations with a constant growth rate can mimic actual phase transformation kinetics correctly. It should be noted that initial austenite grain morphology naturally affects phase proportion rates, as shown in Figure 5(b), hence influencing the transformation strain rate and the resulting transformation plastic strain. This observation is consistent with experimental works [43, 44], wherein different grain morphologies affected final phase proportions.

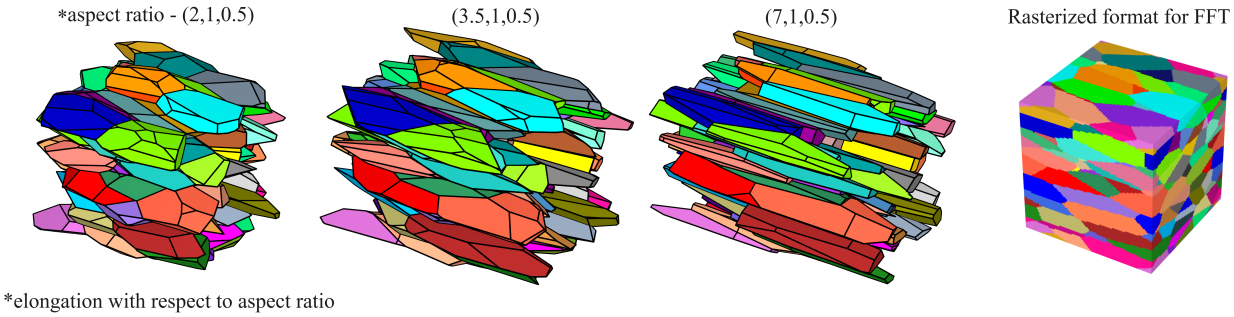

Figure 3: Microstructures with different grain morphologies.

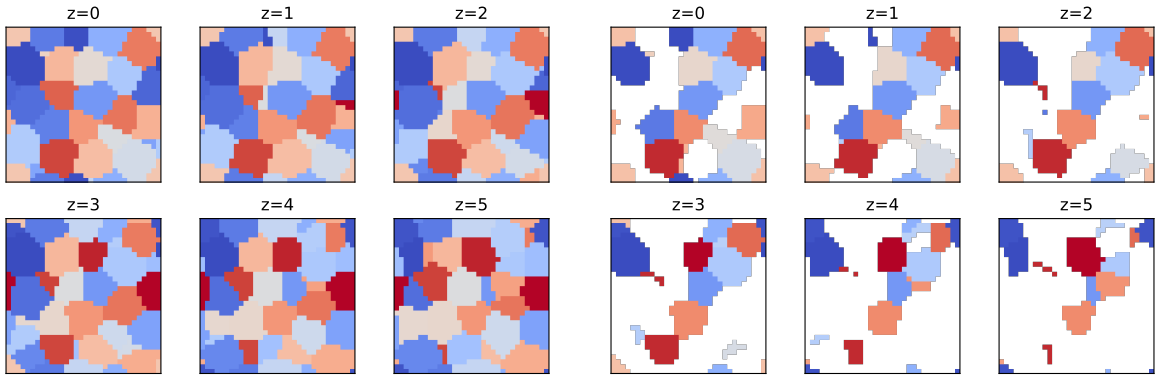

Figure 4: Cross sections of a 3D periodic tessellation at the initial and final states. Austenite grains are shown in color, and ferrite grains in white. (Left) Initial state (i.e., $t = 0$ s and $V_f = 0\%$ and (Right) final state (i.e., $t = 130$ s and $V_f \geq 65\%$).

For one particular oriented tessellation and the different applied loads, the average cumulative plastic strain denoted by P_{cum} derived by integrating (17) is presented as a function of time in Figure 6. The average is considered over austenite grains only in Figure 6(a), ferrite grains only in figure 6(b), and over the entire RVE in Figure 6(c). Since there is no ferrite at $t = 0$ the average over ferrite grains cannot be computed at $t = 0$ and therefore has been discarded in Figure 6(b). A quasi-linear relation is observed for both austenite and ferrite. At the origin, when $t \to 0$

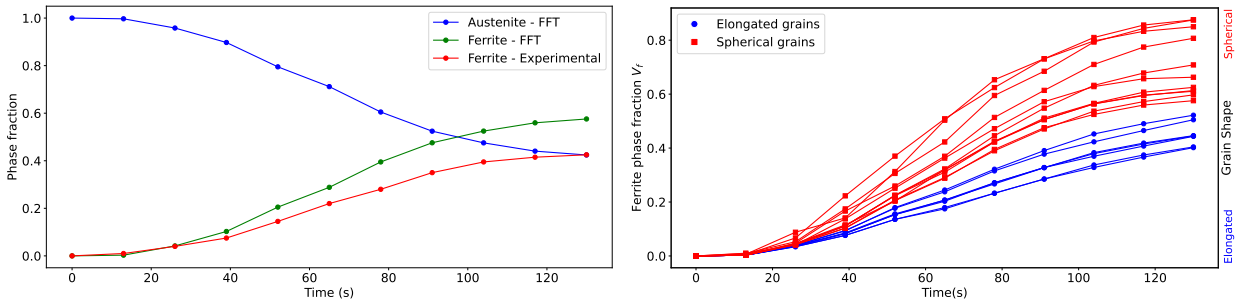

Figure 5: (Left) Evolution of ferrite and austenite phase fractions for one particular computation. (Right) Ferrite phase fraction for spherical and elongated austenite grains.

the cumulative plastic strain P_{cum} converges to zero in austenite while an offset is observed for ferrite. This is explained by the fact that ferrite undergoes plastic deformation throughout its entire volume as soon as phase transformation begins (i.e., at $t = 0$), whereas only an infinitesimal volume fraction of austenite initially undergoes plastic deformation because ferrite nuclei are small inclusions undergoing the transformation strain initially. It should also be noted that the cumulative plastic strain rate $\dot{P}_{\text{cum}}$ (i.e., slopes in figure 6) are non-linearly correlated with the macroscopic applied stress $|\Sigma|$.

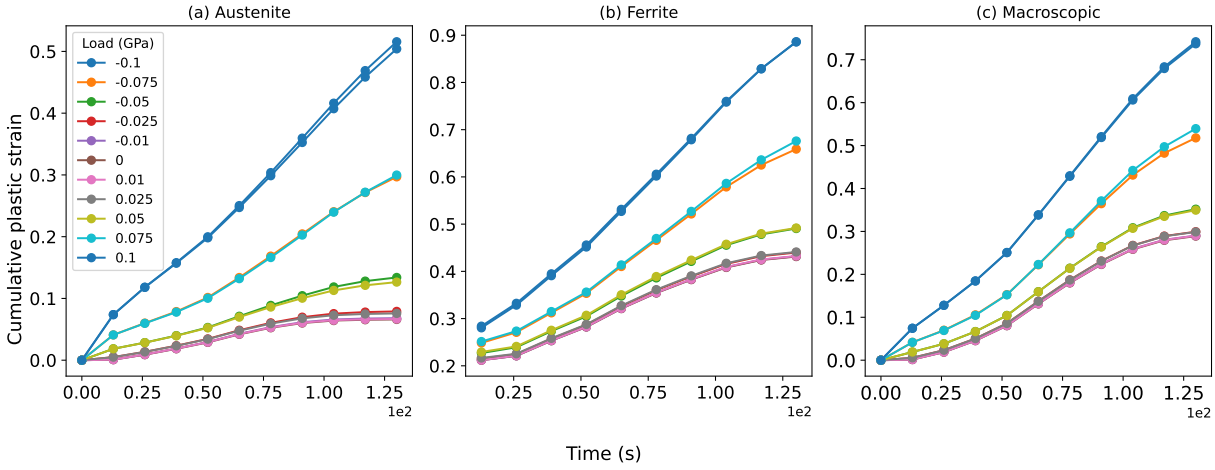

Figure 6: Average cumulative plastic strain P_{cum} as a function of time for different applied loads where averages are considered over (a) austenite grains, (b) ferrite grains, and (c) both austenite and ferrite grains.

In addition, for the same oriented tessellation the average hardening curves are presented for the different macroscopic applied loads in Figure 7. The average equivalent stress denoted by $\Sigma^{\text{eq}} = \sqrt{\frac{3}{2}\boldsymbol{\Sigma}' : \boldsymbol{\Sigma}'}$ (where $\boldsymbol{\Sigma}'$ is the deviator of $\boldsymbol{\Sigma}$) is plotted as a function of the average cumulative plastic strain P_{cum}. The equivalent stress averaged over the entire RVE coincides as expected with the macroscopic boundary condition (i.e., $\Sigma^{\text{eq}} = |\Sigma|$), and the range of P_{cum} is larger for higher macroscopic applied stress $|\Sigma|$ (see. figure 7(c)). Since the initial state is composed of austenite grains only, the equivalent stress averaged over austenite grains starts at the applied macroscopic

stress $|\Sigma|$ as shown in Figure 7(a), while the initial time step is discarded for ferrite at $t = 0$ because there is no ferrite. Then, during phase transformation P_{cum} increases as well as the equivalent stress in both austenite and ferrite. It is clear by comparing Figures 7(a) and (b) that ferrite is indeed softer than austenite. Moreover, on the one hand, the average hardening curves in austenite are S-shaped (i.e., sigmoid functions) as shown in Figure 7(a), which is very different from the hardening curve of pure austenite. This average response may be explained by the fact that the volume fraction undergoing plastic deformation in austenite is more or less proportional to the ferrite phase fraction V_f, which has a typical S-shape with respect to time (see. Figure 5), while the cumulative plastic strain P_{cum} is linear with respect to time as shown in Figure 6. On the other hand, all the ferrite grains undergo plastic deformation as soon as they nucleate and therefore the average hardening curves in ferrite are similar to hardening curves in pure ferrite.

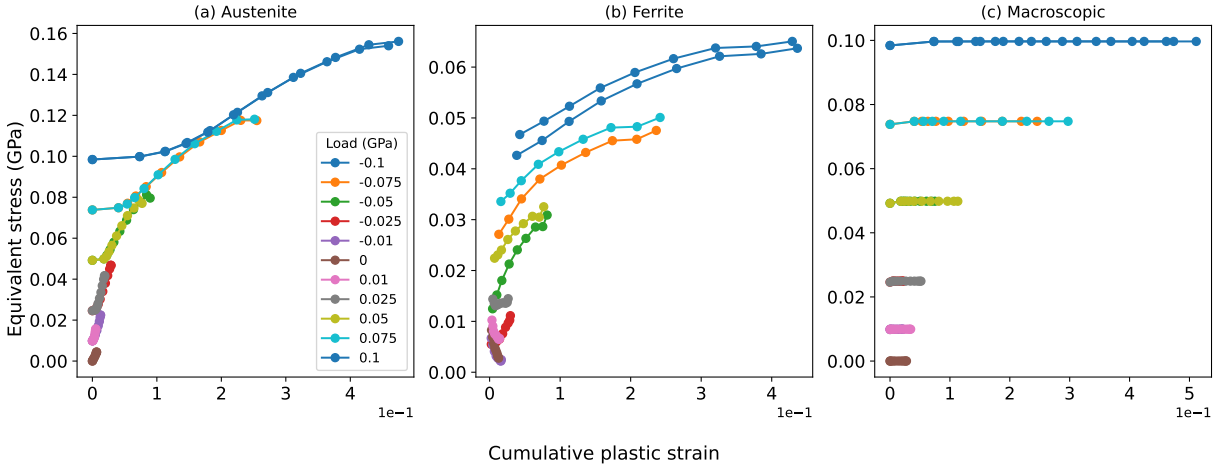

Figure 7: Average equivalent stress as a function of average cumulative plastic strain for different applied loads where averages are considered over (a) austenite grains, (b) ferrite grains, and (c) both austenite and ferrite grains.

Plastic strain is averaged over the entire RVE (i.e., over both austenite and ferrite grains) to capture the overall transformation plastic strain second-order tensor denoted by $\boldsymbol{E}^{\text{tp}}$ defined in (16). In Figure 8, the final transformation plastic strain component E_{11}^{tp} is presented as a function of the applied stress Σ for one particular oriented tessellation. It should be noted that the transformation plastic strain does not vanish when there is no applied stress (i.e., $\Sigma = 0$ MPa). This has been observed for instance in [33] for morphological anisotropy, and is observed in this contribution for crystallographic anisotropy. Indeed, the imposed transformation strain (i.e., the eigenstrain) depends on crystal orientations of the product phase, and therefore a preferential crystal orientation is sufficient for the overall average of local plastic strains not to converge to zero. Since relatively small RVEs are considered (i.e., 100 ferrite grains are formed during phase transformation), crystallographic isotropy is never obtained, and therefore transformation plasticity does not completely vanish for $\Sigma = 0$ MPa. This explanation has been verified by computing an RVE including 500 ferrite grains with an unrealistic condition for which the crystal orientation of ferrite grains is randomly assigned regardless of the parent crystal orientation leading to better crystallographic isotropy. The final transformation plastic strain with $\Sigma = 0$ MPa is reduced

from $E_{11}^{\mathrm{tp}} = 2.12 \times 10^{-2}$ with residual crystallographic anisotropy to $E_{11}^{\mathrm{tp}} = 6.69 \times 10^{-4}$ with better crystallographic isotropy, which represents a reduction higher than 95% hence validating the proposed explanation.

For low applied stress, a linear dependence is observed (i.e., grey zone in Figure 8) while strongly non-linear evolution is obtained for higher applied stress (i.e., red zone in Figure 8) with a smooth transition between linear and non-linear regimes (i.e., white zone in Figure 8). In comparison, as most of the existing analytical models in the literature, the extended Leblond model proposed by Weisz-Patrault [26] predicts a linear relationship between the transformation plastic strain and the applied load. The thresholds between which the relation between the transformation plastic strain and the applied stress becomes strongly non-linear are denoted by $\Sigma_{\mathrm{L}} = 25$ MPa and $\Sigma_{\mathrm{H}} = 50$ MPa (where L and H stand for "low" and "high"). To explain these two regimes (i.e., linear for low applied stress and non-linear for high applied stress) two different mechanisms are suggested:

1) The local transformation strain $\boldsymbol{\varepsilon}^*(\boldsymbol{x})$ always induces plastic deformation in ferrite grains.
2) As shown in Figure 1, applied stresses such as $|\Sigma| \geq \Sigma_{\mathrm{H}}$ are sufficient to reach a quasi-linear regime with low hardening coefficient (i.e., shallow slope) in the hardening curve of austenite at 750°C [34], which therefore induces significant plastic strain in austenite grains to accommodate local deformation induced by ferrite grains on austenite grains.

Accordingly, for low applied stress, only the first mechanism would be activated, while both the first and second mechanisms would be activated for higher applied stress, hence explaining the non-linear variations in Figure 8.

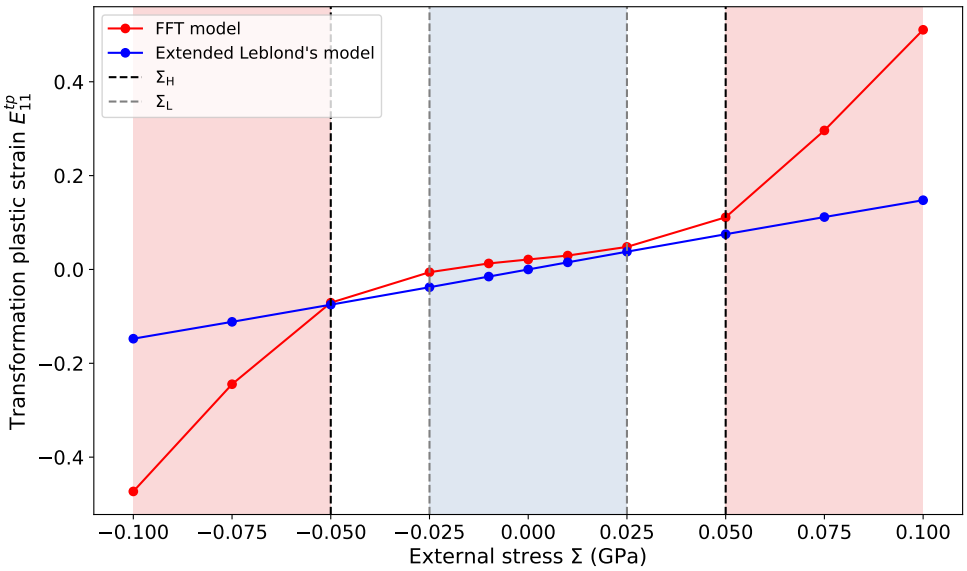

Figure 8: Transformation plastic strain plotted against externally applied stress, compared to the analytical solution (extended Leblond's model [26]

To validate the proposed explanation of the non-linear behavior for large applied stress in Figure 8 involving the combination of the two suggested mechanisms, the average plastic strain

is computed over both ferrite and austenite grains. For instance, in Figure 9 the average plastic strain 11 component is presented for low and high applied stress (i.e., $\Sigma = 10$ MPa (left) and $\Sigma = 100$ MPa (right)) as a function of the product phase fraction V_f. The average is considered over austenite grains (i.e., blue curve), ferrite grains (i.e., green curve), and over the entire RVE (i.e., red curve) which corresponds to the transformation plastic strain component E^{tp}_{11}. On the one hand, for low applied stress (i.e., $\Sigma = 10$ MPa) ferrite grains undergo plastic deformation as soon as the phase transformation begins to accommodate the transformation strain, and one can notice that austenite grains do not undergo significant plastic deformation in average, which corresponds to localized isotropically distributed plastic deformation as demonstrated in the following section. On the other hand, for high applied stress (i.e., $\Sigma = 100$ MPa) not only ferrite grains but also austenite grains undergo significant plastic flow since the applied stress is sufficient to reach the quasi-linear regime of the hardening curve of austenite (see. Figure 1) which induces significant plastic strain in the entire volume of austenite grains. As a result, the transformation plastic strain shows a non-linear growth with respect to the phase fraction for $\Sigma = 100$ MPa while a linear dependence is obtained for $\Sigma = 10$ MPa as only the first mechanism is activated. In fact, between

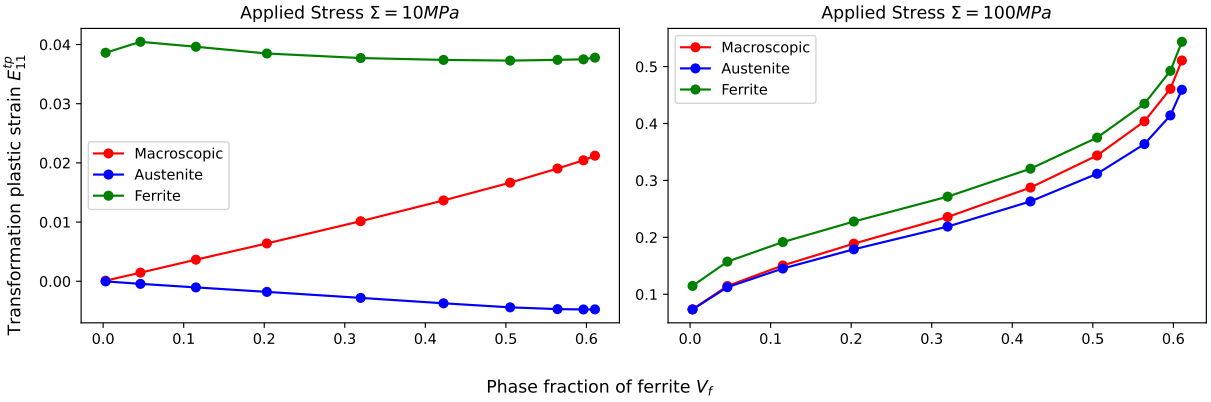

Figure 9: Transformation plastic strain observed with externally applied stresses of 10 MPa (left) and 100 MPa (right) in austenite, ferrite, and averaged macroscopic phase.

low and high applied stress (i.e., especially for $\Sigma_{\mathrm{L}} \leq \Sigma \leq \Sigma_{\mathrm{H}}$) there is a continuous transition in the behavior of the transformation plastic strain. Indeed, since the hardening of austenite is a continuous process starting at the initial yield stress of austenite $\sigma^{\mathrm{Y}}_{\mathrm{aus}} = 12$ MPa, even for low applied load austenite grains undergo uniform plastic strain to accommodate the applied load (i.e., second mechanism) and not only the local deformation imposed by ferrite grains. However, a negligible macroscopic effect is observed for $\Sigma \leq \Sigma_{\mathrm{L}}$. This is due to the fact that the beginning of the hardening curve of austenite is very steep (see. Figure 1), hence the high apparent stiffness of austenite and low associated average plastic strain during the phase transformation. On the contrary, for $\Sigma \geq \Sigma_{\mathrm{H}}$ the slope of the hardening curve of austenite is shallow (see. Figure 1), hence low apparent stiffness of austenite and high associated plastic strain during the phase transformation. This effect is demonstrated in Figure 10 where the average plastic strain component is presented for $\Sigma = \Sigma_{\mathrm{L}}$ (left) and $\Sigma = \Sigma_{\mathrm{H}}$ (right) as a function of the product phase fraction V_f. For $\Sigma = \Sigma_{\mathrm{L}}$ the average plastic strain in austenite grains is strictly positive initially (i.e., $V_f = 0\%$) as the

applied macroscopic stress Σ is higher than the initial yield stress of austenite $\sigma^{\mathrm{Y}}_{\mathrm{aus}}$. However, the average plastic strain in austenite grains increases linearly and rather slowly during the phase transformation, which indicates that the effect of ferrite over austenite is not sufficient to induce significant average plastic strain in austenite grains as the hardening curve of austenite is rather steep. For $\Sigma = \Sigma_{\mathrm{H}}$, during the phase transformation, the growth of the average plastic strain in austenite grains becomes non-linear and more rapid since the slope of the hardening curve of austenite is more shallow.

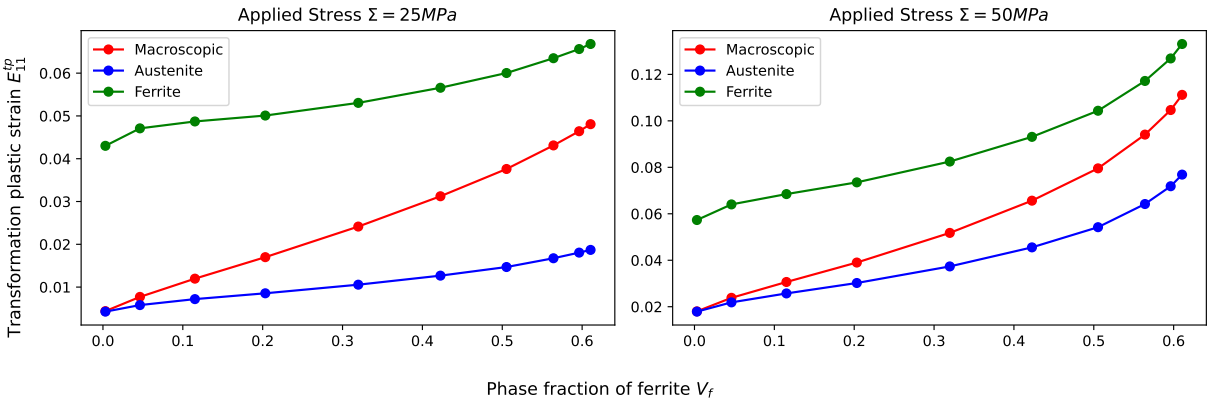

Figure 10: Transformation plastic strain observed with externally applied stresses of 25 MPa (left) and 50 MPa (right) in austenite, ferrite, and averaged macroscopic phase.

3.2.1. Local mechanisms

In this section, the proposed twofold mechanism to explain the nonlinear behavior of transformation plasticity with respect to the applied load is demonstrated in more detail by analyzing local plastic strain fields in both austenite and ferrite grains. In Figures 11 and 12, the local plastic strain component $\varepsilon^{\mathrm{p}}_{11}(\boldsymbol{x})$ is presented at the final time step (i.e., $V_f \approx 65\%$) for different cut planes respectively in ferrite and austenite for a single oriented tessellation. The vertical red lines correspond to the threshold between Σ_{L} and Σ_{H} where the transformation plastic strain becomes non-linear with respect to the applied load. On the one hand, as shown in Figure 11, when the applied stress increases from $\Sigma = 0$ MPa to $\Sigma = 100$ MPa, the plastic strain in ferrite increases especially in grains in which negative plastic strain initially took place (i.e., for $\Sigma = 0$ MPa), which in turn increases the average transformation plastic strain. This mechanism is similar to the Greenwood & Johnson mechanism and can be attributed to the fact that the applied stress favors a specific direction in the plastic flow. This is the only mechanism involved for low applied stress (i.e., $|\Sigma| \leq \Sigma_{\mathrm{L}}$) because austenite grains almost do not undergo plastic deformation and present a uniform plastic strain field due to the external load reaching the yield stress of austenite, as shown in Figure 12. On the other hand, for high applied stress (i.e., $|\Sigma| \geq \Sigma_{\mathrm{H}}$) the yield stress of austenite reaches a quasi-linear regime with low hardening coefficient (see. Figure 1), and therefore austenite grains undergo a significant and almost uniform positive plastic strain according to the loading direction as shown in Figure 12. Indeed, when the applied load is sufficient to reach low hardening, austenite grains naturally undergo plastic strain even without phase transformation, which favors

further plastic flow when the phase transformation starts. Such a mechanism in austenite is added to the Greenwood & Johnson-like mechanism in ferrite, which in turn explains why non-linearity of transformation plasticity with respect to the applied stress develops for high applied stress. As in many other analytical models, the extended Leblond's model [26] was limited to low applied stress because the plastic flow was confined in the parent phase to the very surroundings of the forming grains. This resulted in a linear dependence between the transformation plastic strain and the applied load because the uniform and global plastic flow in the parent phase could not be taken into account for large applied stress as opposed to this contribution.

It should be noted that the Magee mechanism has not been studied in this contribution as the crystal orientation of ferrite nuclei has been selected randomly among the three possible variants.

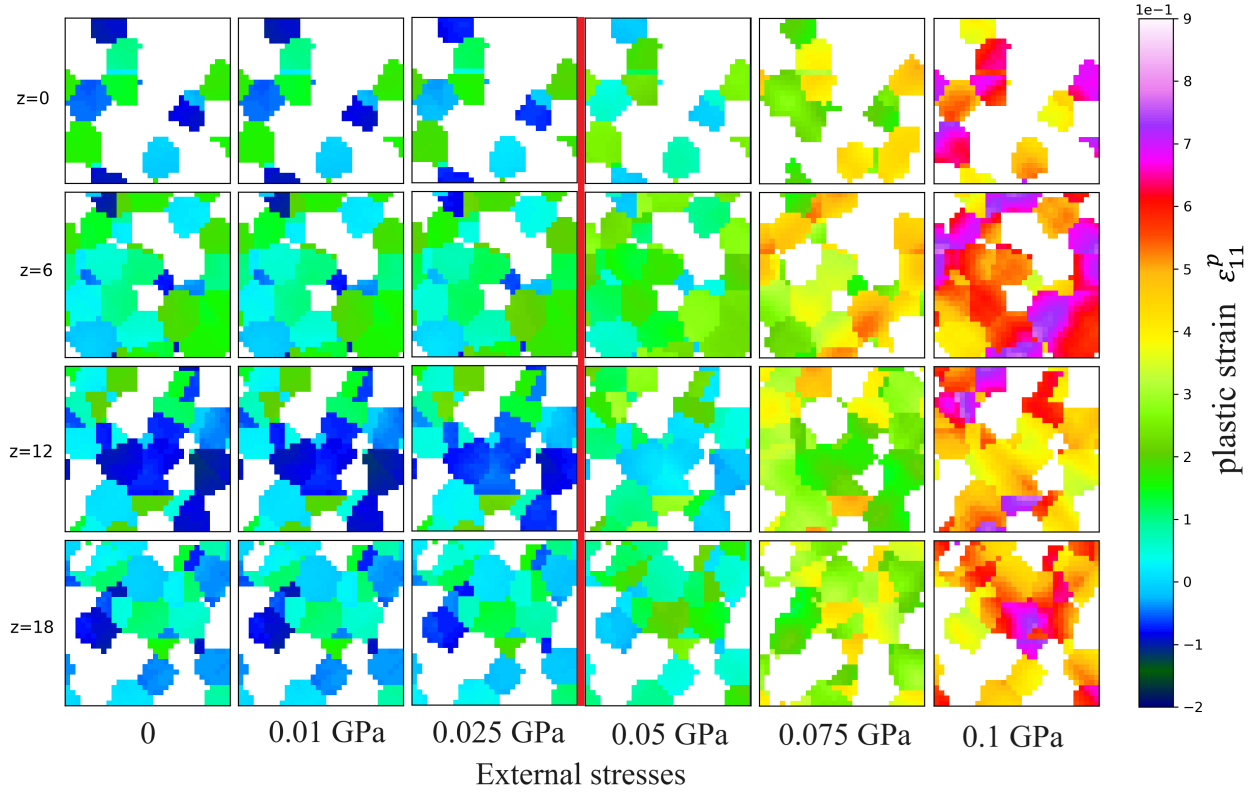

Figure 11: Plastic strain $\varepsilon^{\mathrm{p}}_{11}$ at the final time step for different applied stresses in ferrite grains. The red line corresponds to the threshold Σ_{c}.

3.3. Macroscopic statistical model of transformation plasticity

In this section, the database of FFTcomputations introduced in section 3.1 is exploited to derive a macroscopic statistical model of transformation plasticity. Of course, the resulting macroscopic model is only valid for the selected elasto-visco-plastic behavior and material properties. But the proposed methodology could be used for other materials.

In Figure 13, the transformation plastic strain component E^{tp}_{11} is plotted against the volume phase fraction V_f and applied stress Σ for all the 1452 data points (i.e., for the 12 oriented tessellations, the

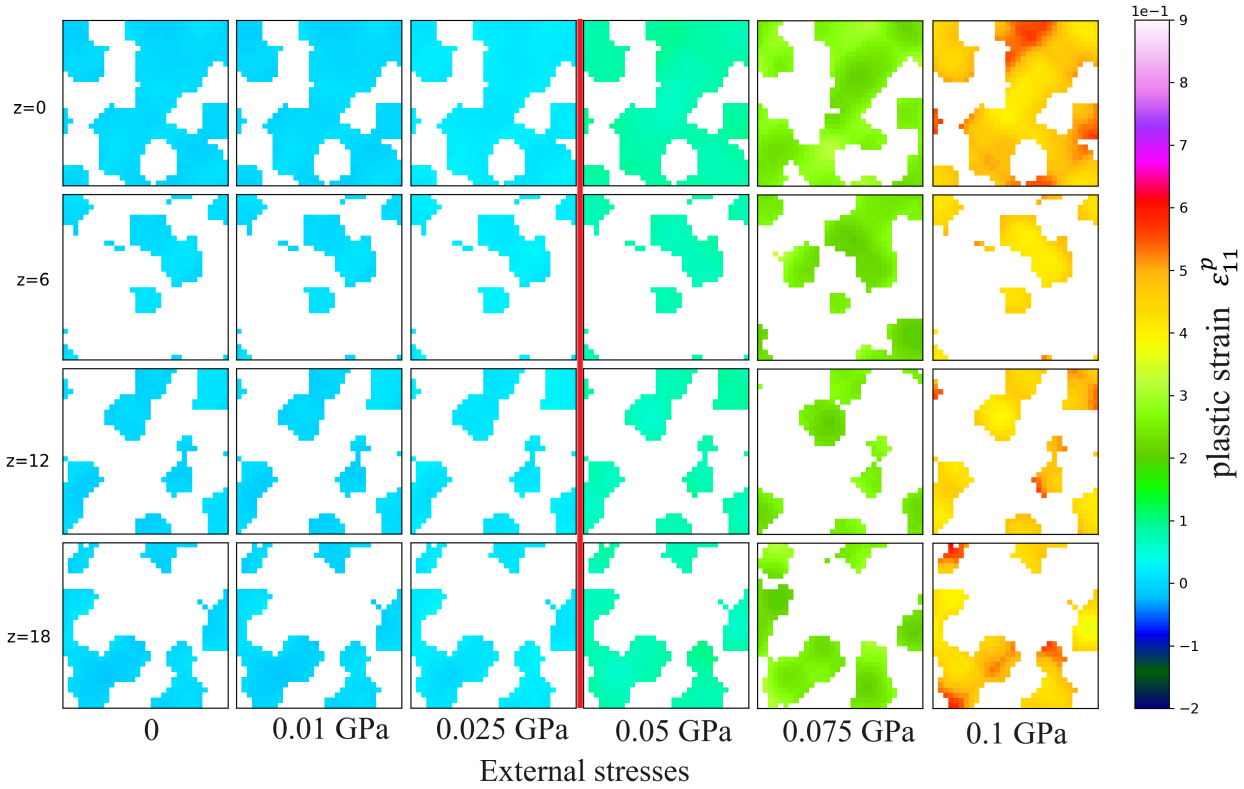

Figure 12: Transformation plastic strain $\varepsilon^{\mathrm{p}}_{11}$ at the final time step for different applied stresses in austenite grains. The red line corresponds to the threshold Σ_{c}.

11 applied stresses Σ, and for the 11 recorded time steps during phase transformation). The volume phase fraction V_f and the applied stress Σ are the two main state variables explaining transformation plasticity as one can observe a quasi-deterministic distribution of E^{tp}_{11} with limited dispersion of data for each pair (V_f, Σ) in Figure 13. The dispersion could be attributed to the effect of strain rate, and morphological texture (e.g., oriented tessellations with different grain shape distributions have been included in the data set). It should be noted that the effect of crystallographic texture of the initial fully austenitic microstructure has not been tested though, since crystal orientations of austenite grains are randomly selected using a uniform distribution.

Since visco-plastic behavior is considered, the macroscopic statistical model is derived in rates to take into account non-linear evolution. The phase fraction rate $\dot{V}_f$ is therefore added to the two-state variables already considered: namely the applied stress Σ and the volume phase fraction V_f. It should be noted that $\dot{\Sigma}$ is not considered in this study as constant applied stress has been applied. In Figure 14, the transformation plastic strain rate component $\dot{E}^{\mathrm{tp}}_{11}$ is presented for all the oriented tessellations in the database and $\Sigma = 0.1$ GPa as a function of the volume phase fraction V_f and its rate $\dot{V}_f$. Similar results are obtained for other applied loads. A quasi-deterministic distribution is obtained, which indicates that the chosen state variables are sufficient to capture transformation plasticity at the macroscopic scale without introducing significant epistemic uncertainty [36]. A polynomial regression of degree 2 is considered to interpolate data points with an average relative

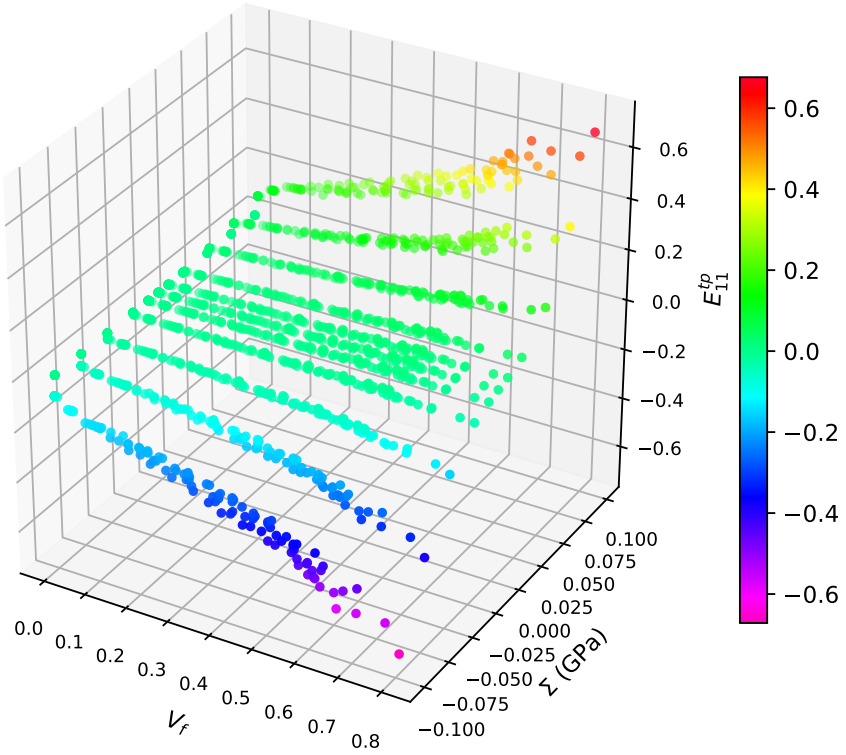

Figure 13: Transformation plastic strain component E_{11}^{tp} against externally applied stress Σ and volume phase fraction V_f.

error of 10%. Hence, computing the polynomial regression for all applied loads, the macroscopic model reads:

$$\dot{E}_{11}^{\mathrm{tp}} = A(\Sigma)\,\left(1 + \alpha_1\,\dot{V}_f + \beta_1\,V_f + \alpha_2\,\dot{V}_f^2 + \beta_2\,V_f^2 + \gamma\,\dot{V}_f\,V_f\right) \tag{19}$$

where $\alpha_1, \beta_1, \alpha_2, \beta_2, \gamma$ are listed in Table 3. In addition, A is presented as a function of Σ in Figure 15. Since the applied stress tensor is written in the form $\boldsymbol{\Sigma} = \Sigma\,\boldsymbol{e}_1 \otimes \boldsymbol{e}_1$, other transformation plastic strain rate components read $\dot{E}_{22}^{\mathrm{tp}} \approx \dot{E}_{33}^{\mathrm{tp}} \approx -\dot{E}_{11}^{\mathrm{tp}}/2$ and $\dot{E}_{12}^{\mathrm{tp}} \approx \dot{E}_{13}^{\mathrm{tp}} \approx \dot{E}_{23}^{\mathrm{tp}} \approx 0$. A polynomial regression of degree 3 is proposed such as:

$$A(\Sigma) = A_0 + A_1\,\Sigma + A_2\,\Sigma^2 + A_3\,\Sigma^3 \tag{20}$$

where coefficients A_0, A_1, A_2, A_3 are listed in Table 4.

3.4. Validation of the macroscopic statistical model

The macroscopic statistical model derived in (19) and (20) is validated in this section. Numerical predictions of the overall transformation plastic strain evolution are compared with detailed FFT - based computations at the mesoscopic scale using oriented tessellations that have not been included in the database. The considered applied loads are $\Sigma = -0.075, 0.05, 0.1$ GPa, and the volume

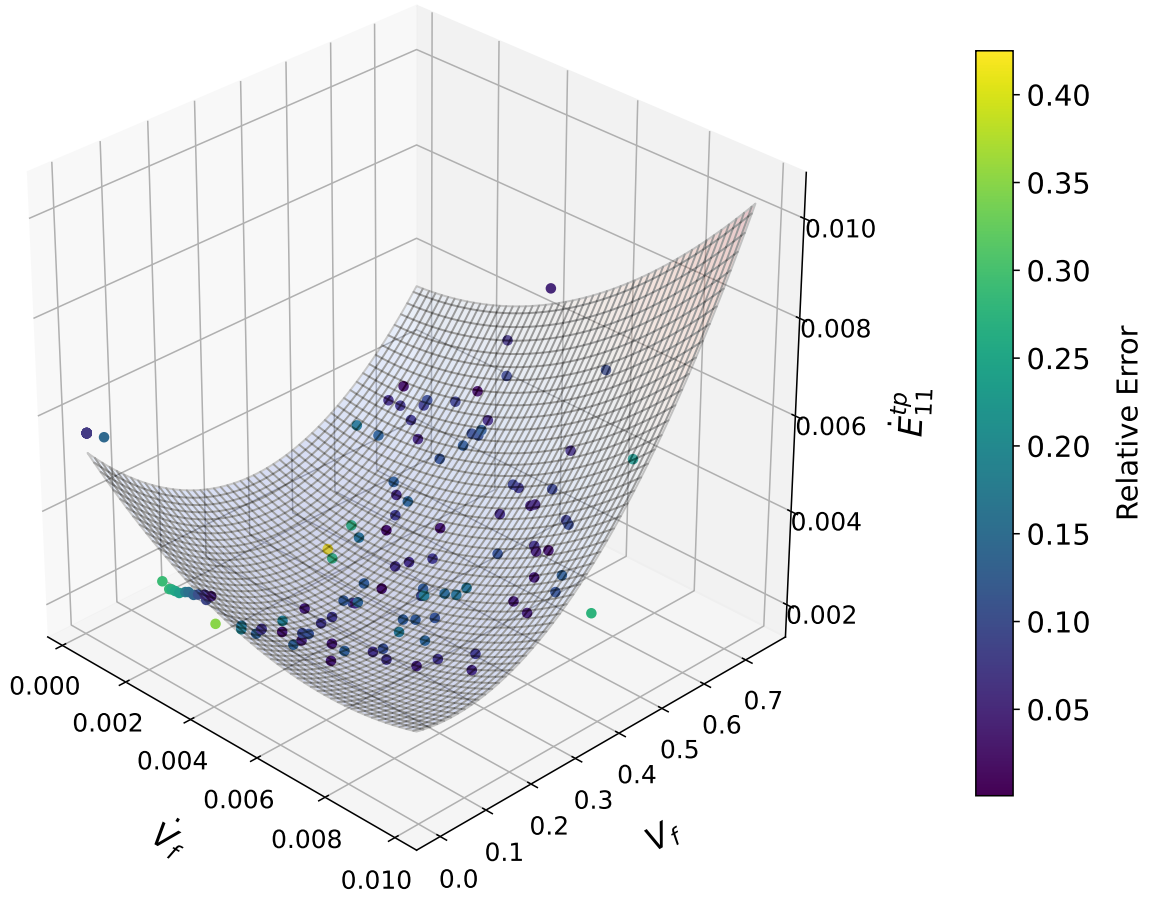

Figure 14: Transformation plastic strain rate component $\dot{E}_{11}^{\mathrm{tp}}$ given in s^{-1} including all oriented tessellations in the database plotted as a function of the volume phase proportion V_f and its rate $\dot{V}_f$ for $\Sigma = 100$ MPa. A polynomial regression of degree 2 is plotted with relative errors.

Table 3: Coefficients of the polynomial regression (19).

α_1	(s^{-1})	-155.15
α_2	(s^{-2})	9012.72
β_1	(-)	-2.51
β_2	(-)	3.32
γ	(s^{-1})	251.22

phase fraction V_f and its rate $\dot{V}_f$ is extracted from the mesoscale computations and used in the macroscopic computation.

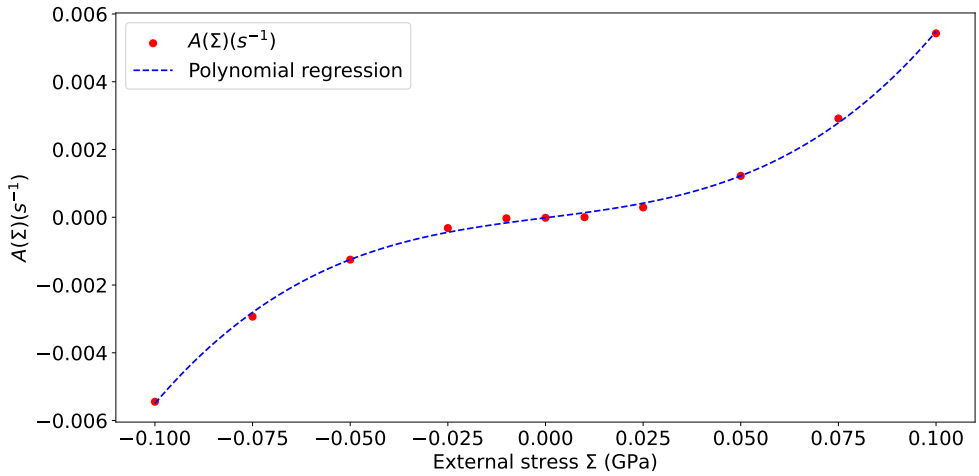

Figure 15: $A(\Sigma)$ as a function of the applied load Σ with a polynomial regression of degree 3.

Table 4: Coefficients of the polynomial regression (20).

A_0	(s^{-1})	-1.499×10^{-5}
A_1	(s^{-1}.GPa^{-1})	1.465×10^{-2}
A_2	(s^{-1}.GPa^{-2})	7.492×10^{-4}
A_3	(s^{-1}.GPa^{-3})	4.023

The comparison is presented in Figure 16, and satisfying agreement is observed, which demonstrates how a relatively small database of mesoscale computations can be used to derive a macroscopic model of transformation plasticity. Of course, the proposed macroscopic model strongly depends on the chosen behavior, which is temperature and material-dependent. Stress triaxiality has not been considered in the model, but the same methodology could be applied. In addition, only isotropically distributed crystal orientations have been tested for initial austenite grains, and therefore the proposed model does not depend on statistical descriptors of the crystallographic texture. In contrast, different morphological textures have been included in the database (with more or less elongated grains) with no significant macroscopic effect.

4. Conclusion

In this contribution, transformation plasticity has been investigated by using FFT based simulations of polycrystals undergoing phase transformation under various applied loads. The $\gamma \rightarrow \alpha$ phase transformation is considered in steel under isothermal conditions at $T = 750°$C. The elasto-viscoplastic behavior has been considered and the parent phase (austenite) is harder than the product phase (ferrite). In addition, the transformation strain and orientation relationship between ferrite and austenite is determined by using the Bain mechanism.

Results show that the transformation plastic strain is highly non-linear with respect to the applied load and the volume phase fraction. Two main mechanisms based on average and local analysis of the plastic strain fields have been identified to explain such a non-linear response.

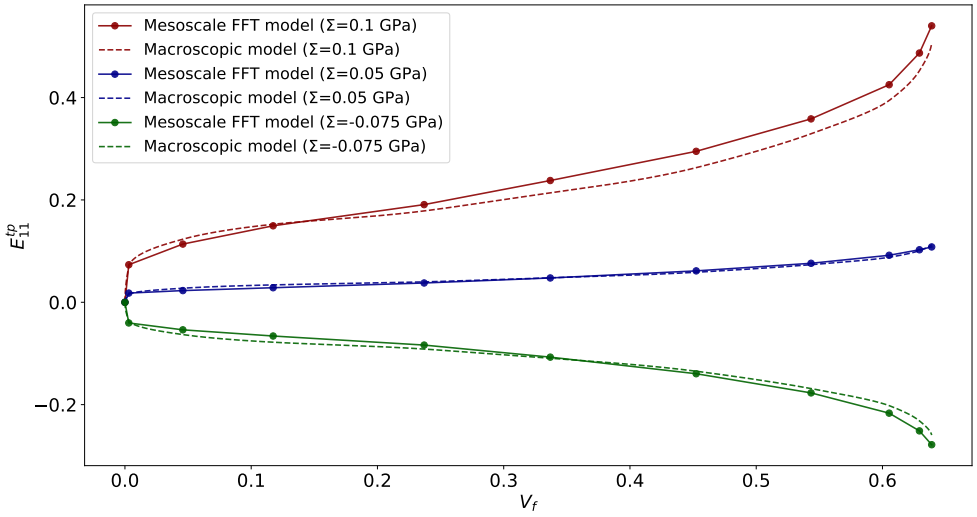

Figure 16: Validation of macroscopic model against a mesoscale numerical simulation with external stress $\Sigma = 0.1, 0.05, -0.075$ GPa.

In addition, a database of FFT computations has been produced to derive a macroscopic statistical model in order to upscale transformation plasticity including the complex non-linear behavior missing in well-known analytical formulas. The obtained model gives the transformation plastic strain rate as a function of three state variables, namely the applied stress, the volume phase fraction, and the volume phase fraction rate. Satisfying agreement is observed between the macroscopic statistical model and FFT computations that have not been included in the database. The proposed methodology shows that relatively small databases that involve relatively fast computations based on FFT algorithms at the mesoscopic scale (i.e., polycrystal), enable to derive accurate macroscopic models, which in turn can be used in large-scale simulations.

References

[1] G. Totten, M. Howes, T. Inoue, Residual Stress Formation Processes during Welding and Joining, 2002.

[2] D. Weisz-Patrault, T. Koedinger, Residual stress on the run out table accounting for multiphase transitions and transformation induced plasticity, Applied Mathematical Modelling 60 (2018) 18–33.

[3] D. Weisz-Patrault, Nonlinear and multiphysics evaluation of residual stresses in coils, Applied Mathematical Modelling 61 (2018) 141–166.

[4] J. Molleda, R. Usamentiaga, D. F. García, On-line flatness measurement in the steelmaking industry, Sensors (Switzerland) 13 (2013) 10245–10272.

[5] B. Anderssen, N. Fowkes, R. Hickson, M. McGuinness, Analysis of coil slumping, Proceedings of the 2009 Mathematics in Industry Study Group (2010) 90–108.

[6] D. Weisz-Patrault, M. Gantier, A. Ehrlacher, Mixed analytic/energetic approach for a sliding orthotropic hollow cylinder. application to coil sagging, International Journal of Solids and Structures 165 (2019) 75–92.

[7] E. Gautier, J. S. Zhang, X. M. Zhang, Martensitic Transformation under Stress in Ferrous Alloys. Mechanical Behaviour and Resulting Morphologies, Le Journal de Physique IV 05 (1995) C8–41–C8–50.

[8] L. Taleb, N. Cavallo, F. Waeckel, Experimental analysis of transformation plasticity, International journal of plasticity 17 (2001) 1–20.

[9] M. Coret, S. Calloch, A. Combescure, Experimental study of the phase transformation plasticity of 16MND5 low

carbon steel induced by proportional and nonproportional biaxial loading paths, European Journal of Mechanics, A/Solids 23 (2004) 823–842.
[10] M. Coret, S. Calloch, A. Combescure, Experimental study of the phase transformation plasticity of 16mnd5 low carbon steel under multiaxial loading, International Journal of Plasticity 18 (2002) 1707–1727.
[11] L. Taleb, S. Petit, New investigations on transformation induced plasticity and its interaction with classical plasticity, International journal of plasticity 22 (2006) 110–130.
[12] J. B. Leblond, G. Mottet, J. C. Devaux, A theoretical and numerical approach to the plastic behaviour of steels during phase transformations-I. Derivation of general relations, Journal of the Mechanics and Physics of Solids 34 (1986) 395–409.
[13] J. B. Leblond, J. Devaux, J. C. Devaux, Mathematical modelling of transformation plasticity in steels I: Case of ideal-plastic phases, International Journal of Plasticity 5 (1989) 551–572.
[14] F. D. Fischer, A micromechanical model for transformation plasticity in steels, Acta Metallurgica et Materialia 38 (1990) 1535–1546.
[15] F. D. Fischer, G. Reisner, E. Werner, K. Tanaka, G. Cailletaud, T. Antretter, A new view on transformation induced plasticity (trip), International Journal of Plasticity 16 (2000) 723–748.
[16] Jean-François Ganghoffer, Elisabeth Aeby-Gautie, S. Denis, S. Sjöström, Martensitic transformation plasticity simulations by finite elements, Journal de Physique IV (Proceedings) (1994).
[17] J. F. Ganghoffer, S. Denis, E. Gautier, S. Sjöström, Micromechanical analysis of the finite element calculation of a diffusional transformation, Journal of Materials Science 32 (1997) 4941–4955.
[18] J. F. Ganghoffer, K. Simonsson, A micromechanical model of the martensitic transformation, Mechanics of Materials 27 (1998) 125–144.
[19] J. M. Diani, H. Sabar, M. Berveiller, Micromechanical modelling of the transformation induced plasticity (trip) phenomenon in steels, International Journal of Engineering Science 33 (1995) 1921–1934.
[20] C. Schuh, D. C. Dunand, An overview of power-law creep in polycrystalline β-titanium, Scripta Materialia 45 (2001) 1415–1421.
[21] S. Denis, P. Archambault, E. Gautier, A. Simon, G. Beck, Prediction of residual stress and distortion of ferrous and non-ferrous metals: Current status and future developments, Journal of Materials Engineering and Performance 11 (2002) 92–102.
[22] Y. Vincent, J. M. Bergheau, J. B. Leblond, Viscoplastic behaviour of steels during phase transformations, Comptes Rendus - Mecanique 331 (2003) 587–594.
[23] L. Taleb, F. Sidoroff, A micromechanical modeling of the Greenwood-Johnson mechanism in transformation induced plasticity, International Journal of Plasticity 19 (2003) 1821–1842.
[24] T. Iwamoto, Multiscale computational simulation of deformation behavior of trip steel with growth of martensitic particles in unit cell by asymptotic homogenization method, International Journal of Plasticity 4-5 (2004) 841–869.
[25] F. Barbe, R. Quey, L. Taleb, Numerical modelling of the plasticity induced during diffusive transformation. Case of a cubic array of nuclei, European Journal of Mechanics, A/Solids 26 (2007) 611–625.
[26] D. Weisz-Patrault, Multiphase model for transformation induced plasticity. Extended Leblond's model, Journal of the Mechanics and Physics of Solids 106 (2017) 152–175.
[27] Y. E. Majaty, J. B. Leblond, D. Kondo, A novel treatment of Greenwood–Johnson's mechanism of transformation plasticity - Case of spherical growth of nuclei of daughter-phase, Journal of the Mechanics and Physics of Solids 121 (2018) 175–197.
[28] G. W. Greenwood, R. H. Johnson, The deformation of metals under small stresses during phase transformations, Proceedings of the Royal Society of London. Series A. Mathematical and Physical Sciences 283 (1965) 403–422.
[29] C. L. Magee, Transformation kinetics, microplasticity and aging of martensite in Fe-31 Ni, Ph.D. thesis, Ph. D. Thesis, Carnegie Institute of Technology, Pittsburgh, 1966.
[30] F. Barbe, R. Quey, A numerical modelling of 3D polycrystal-to-polycrystal diffusive phase transformations involving crystal plasticity, International Journal of Plasticity 27 (2011) 823–840.
[31] T. Otsuka, R. Brenner, B. Bacroix, FFT-based modelling of transformation plasticity in polycrystalline materials during diffusive phase transformation, International Journal of Engineering Science 127 (2018) 92–113.
[32] Y. El Majaty, R. Brenner, J. B. Leblond, FFT-based micromechanical simulations of transformation plasticity.

Comparison with a limit-analysis-based theory, European Journal of Mechanics, A/Solids 86 (2021) 104152.
[33] Y. El Majaty, L.-H. Tran, J.-B. Leblond, R. Brenner, Modeling the effects of morphological anisotropy in transformation plasticity of metals and alloys, International Journal of Solids and Structures 282 (2023) 112447.
[34] C. Liebaut, Rheologie de la déformation plastique d'un acier Fe-C durant sa transformation de phase austenite to ferrite and perlite, Ph.D. thesis, Thèse de doctorat dirigée par Simon, André Mécanique Vandoeuvre-les-Nancy, INPL 1988, 1988.
[35] S. Sakout, D. Weisz-Patrault, A. Ehrlacher, Energetic upscaling strategy for grain growth. I: Fast mesoscopic model based on dissipation, Acta Materialia 196 (2020) 261–279.
[36] D. Weisz-Patrault, S. Sakout, A. Ehrlacher, Energetic upscaling strategy for grain growth. II: Probabilistic macroscopic model identified by bayesian techniques, Acta Materialia 210 (2021) 116805.
[37] H. Moulinec, P. Suquet, A fast numerical method for computing the linear and nonlinear mechanical properties of composites, Comptes Rendus de l'Académie des Sciences. Série II, Mécanique, Physique, Chimie, Sciences de l'Univers, Sciences de la Terre 318 (1994) 1417–1423.
[38] J.-L. Chaboche, Constitutive equations for cyclic plasticity and cyclic viscoplasticity, International Journal of Plasticity 7 (1991) 551–571.
[39] A. Matsuzaki, H. Bhadeshia, H. Harada, Stress affected bainitic transformation in a fe c si mn alloy, Acta metallurgica et materialia 42 (1994) 1081–1090.
[40] H. Moulinec, P. Suquet, A numerical method for computing the overall response of nonlinear composites with complex microstructure, Computer Methods in Applied Mechanics and Engineering 157 (1998) 69–94.
[41] R. Quey, E. Hug, P. Suquet, Neper, Computer Physics Communications 180 (2009) 908–922.
[42] E. Gamsjäger, J. Svoboda, F. Fischer, Austenite-to-ferrite phase transformation in low-alloyed steels, Computational Materials Science 32 (2005) 360–369. IWCMM.
[43] Y. Shen, L. Qiu, X. Sun, L. Zuo, P. Liaw, D. Raabe, Effects of retained austenite volume fraction, morphology, and carbon content on strength and ductility of nanostructured trip-assisted steels, Materials Science and Engineering: A 636 (2015) 551–564.
[44] A.-P. Pierman, O. Bouaziz, T. Pardoen, P. Jacques, L. Brassart, The influence of microstructure and composition on the plastic behaviour of dual-phase steels, Acta Materialia 73 (2014) 298–311.